The Meteoritical Society

Meteoritics & Planetary Science 57, Nr 5, 1098–1115 (2022)
doi: 10.1111/maps.13810

Olivine aggregates reveal a complex collisional history of the main group pallasite parent body

Nicolas P. WALTE *[1], and Gregor J. GOLABEK [2]

[1]Heinz Maier-Leibnitz Center for Neutron Science (MLZ), Technical University Munich, Garching 85748, Germany
[2]Bayerisches Geoinstitut (BGI), University of Bayreuth, Bayreuth 95447, Germany
*Corresponding author. E-mail: nicolas.walte@frm2.tum.de

(Received 01 December 2021; Revised 23, February 2022; revision accepted 07 March 2022)

Abstract–Olivine aggregates, bodies found in pallasites that consist of olivines with coherent grain boundaries and minor amounts of Fe-Ni and troilite, likely represent well-preserved samples of different mantle regions of pallasite parent bodies (PPBs). We investigated olivine aggregates from the main group pallasites Fukang, Esquel, Imilac, and Seymchan and compare their textures with results from deformation experiments. Our measurements reveal an inverse relationship between the grain size of olivines and the primary metal fraction inside olivine aggregates, which is explained by simultaneous grain growth retarded by Zener pinning in different mantle regions. Textural evidence indicates that the mantle has remained at high temperatures before initial cooling occurred shortly after pallasite formation that was likely caused by an impact. Different degrees of annealing of the deformation textures suggest that the postcollisional cooling occurred in the order Seymchan, Imilac, Esquel, and Fukang. We interpret this observation with an increasing burial depth after the collision. We also demonstrate that the mantle has not been convecting before the impact despite being at high temperature. Using the minimum critical Rayleigh number, we estimate PPB radii assuming different core radii. Our results question the recent ferromagmatism hypothesis for pallasite formation and support a multistage formation process that includes one or several impacts.

INTRODUCTION

Pallasites, stony-iron meteorites that are mainly composed of large olivine grains embedded in a matrix of Fe-Ni metal, provide one of the sparse sources of dunitic mantle material from planetesimals in the meteorite record (e.g., Greenwood et al., 2015). However, their use for systematic investigation of the deep interior of planetesimals is impaired by their enigmatic composition and an ongoing controversy regarding their formation depth and formation conditions (e.g., Boesenberg et al., 2012; DellaGiustina et al., 2019; Johnson et al., 2020; McKibbin et al., 2019; Tarduno et al., 2012; Walte et al., 2020; Yang et al., 2010). An important role for deciphering these events is played by olivine aggregates, the texturally oldest components of pallasites that have the closest connection to their host rock (Scott, 1977, 2017; Walte et al., 2020). Olivine aggregates, also termed olivine masses (Scott, 1977), olivine nodules (Ulff-Møller et al., 1998), or olivine clusters (Boesenberg et al., 2012), are groups of olivines with cohesive grain boundaries that contain a lower fraction of Fe-Ni metal and troilite (FeS) than the adjacent pallasite regions (Fig. 1). If defined in such a broad manner, all angular or fragmental pallasites contain olivine aggregates ranging in size from <1 cm up to several decimeters across.

While it was already shown decades ago that olivine aggregates are relicts of the source rock of pallasites (Scott, 1977), their nature and origin remained elusive, either representing olivine cumulates (e.g., Buseck, 1977) or restites (Boesenberg et al., 2012; Walte et al., 2020). Recent modeling studies of olivine trace elements have confirmed a restitic nature of pallasite olivines as remnants of high-grade fractional melt removal, which is compatible with planetesimal differentiation by partial melting and

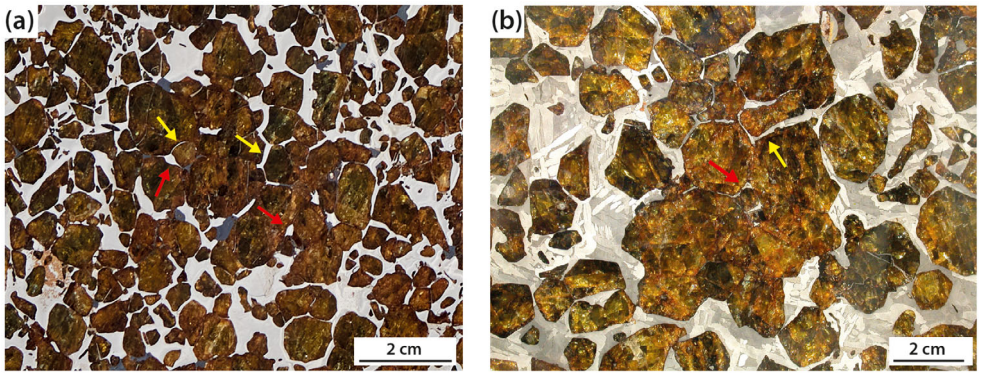

Fig. 1. Olivine aggregates of (a) Imilac and (b) Fukang pallasites. Red arrows denote primary metal pockets and yellow arrows denote secondary veinlets (intergranular fractures, cf. Scott, 1977). a) Detail of BM.53322. © The Trustees of the National History Museum, London. b) Detail of Fukang main mass. Credit: Dolores Hill, University of Arizona, Lunar & Planetary Laboratory. (Color figure can be viewed at wileyonlinelibrary.com.)

melt transport rather than with crystallization from a deep magma ocean (Barrat & Ferrière, 2021). Additionally, a series of studies from the last decade located pallasites firmly in the middle mantle (Bryson et al., 2015; Tarduno et al., 2012; Yang et al., 2010) or even closer to the surface (Walte et al., 2020) indicating that olivine aggregates present true and possibly representative mantle samples. In the current study, we present a textural investigation of olivine aggregates contained in the main group (MG) pallasites Seymchan, Esquel, Imilac, and Fukang. The oxygen data of MG pallasites indicate that they originate from a common parent body (e.g., Greenwood et al., 2015; Wasson & Choi, 2003; Yang et al., 2010). This makes them ideal for this study as they may thereby sample different mantle regions of a single body. We report properties such as grain size, the degree of textural equilibration, olivine–metal textures, and the volume fraction of metal and troilite pockets. In addition, we distinguish between primary features and the textural overprint by the later pallasite formation event, and finally consider postevent textural modifications. Based on our results, we reaffirm the formation of pallasites by a non-destructive two-body collision, explain the grain-size differences between pallasites, make inferences about the relative burial depths of the pallasites immediately after their formation, and give upper limits for the size of the pallasite parent body (PPB) assuming different core radii.

Olivine Aggregates and the Formation of Olivine–Metal Textures

> *These pallasites contain evidence for three distinct events in the formation of pallasitic olivine-metal textures; (1) the fracture of parental, polycrystalline, olivine masses up to at least 30 cm in size, (2) introduction of metal, which frequently separated and reoriented the fragments of the olivine masses during mixing, and (3) migration of olivine-metal boundaries during annealing. (Scott, 1977)*

The three events for creating pallasite textures from olivine aggregates described by Scott (1977) more than four decades ago are still valid (Walte et al., 2020) and serve as a framework for the present work. Following up on the description of metal-filled fractures created during the pallasite formation event (event [1-2] of Scott, 1977) and of roundish Fe-Ni and troilite pockets (Ulff-Møller et al., 1998), Walte et al. (2020) distinguished between two olivine–metal textures that are found inside natural and synthetic olivine aggregates from pallasites and deformation experiments, respectively (Figs. 1 and see 7a). (i) Often equiaxed metal and/or troilite pockets whose shape is determined by surface energy equilibration. Because they predate the pallasite formation event (Ulff-Møller et al., 1998; Walte et al., 2020), they were termed "primordial" (cf. Walte et al., 2020). For the present work and based on the results presented in this study, we use the descriptive term "primary metal pockets" or "primary metal." (ii) Fe-Ni metal and troilite-filled fractures and veinlets that often follow olivine grain boundaries (intergranular fractures, cf. Scott, 1977) that are not equilibrated with respect to metal–olivine surface energies, and are thought to preserve the initial stage of disaggregation by extensional deformation during pallasite formation (Scott, 1977; Walte et al., 2020). In the following text, we will use the term "secondary features" for such metal-filled fractures and veinlets to distinguish them from the primary metal pockets.

Table 1. Summary of investigated pallasite samples.

Pallasite name	Collection no.	Source	Dimensions (cm)	Olivine grain size $d_{olivine}$ (mm)[a]	Primary metal fraction f_{metal}[b]	Primary metal pocket size d_{metal} (mm)	Overview image
Seymchan	#5168	AMNH	52 × 44	*NA*	0.11	3.6	Fig. 1 of Walte et al. (2020)
Seymchan	SEY-18-01	Private collection	20 × 14	3.9	0.09–0.1	2.8	Fig. S1, Fig. 1 of Walte et al. (2020)
Imilac	BM.53322	NHM	54 × 46	6.5	0.08	3.4	Fig. S2
Esquel	G.2010.9.1	NMS	26.5 × 25	7.8	0.028–0.031	*NA*	Fig. S1
Esquel	#4972	AMNH	36 × 21	8.4	0.027–0.05	2.3	Fig. S3
Esquel	#4958	AMNH	84 × 36	8.7	0.042	3.1	Fig. S4
Fukang	Main mass Fukang[c]	Univ. Arizona	95 × 45	13–15	0.015–0.025	3.1	Fig. S5

AMNH = American Museum of Natural History, New York, NY, USA; NHM = Natural History Museum, London, UK; NMS = National Museums of Scotland, Edinburgh, Scotland, UK; Univ. Arizona = University of Arizona, Lunar & Planetary Laboratory, Tucson, AZ, USA.
[a]Average grain size determined from olivine aggregates as detailed in the Methods section.
[b]Volume fraction of equilibrated Fe-Ni and troilite metal pockets that are contained inside olivine aggregates. Note that this fraction is unrelated to the overall olivine–Fe-Ni-S ratio of the pallasite.
[c]Property of Marvin and Kitty Killgore of Southwest Meteorite Lab.

SAMPLES AND METHODS

Pallasite Samples

With the exception of the Seymchan pallasite sample SEY-18-01 that was physically available for this study, all investigations were based on high-quality photographic images of pallasite sections that were provided by the curators and scientists attached to natural history museums and collections that host the slabs as summarized in Table 1. The sample selection was based on the size and quality of the specimens and of the olivine aggregates contained in the samples as well as on the availability of the samples for research. By visually comparing the samples to other published and unpublished images of pallasites it was ensured that the chosen material represents typical examples, while being exceptional only in terms of the area of exposed pallasite textures and the lack of secondary alteration that allowed the detailed textural analyses based on high resolution optical images. For the current study, only angular pallasites were used, because no high-quality images of sufficiently large and unweathered samples of fragmental pallasites such as Admire were available. Likewise, we did not investigate round-type pallasites such as Brenham, because grain-size analyses and textural investigations were already performed by Solferino et al. (2015). For each of the four MG pallasites 2–6, olivine aggregates with diameters of 5–18 cm were analyzed based on optical images of one to three polished sections (Table 1; see Figs. S1–S5 in the supporting information for overview images of the analyzed sections). The resolution of the optical images allowed distinguishing details measuring ≈100 μm and larger; for Seymchan sample SEY-18-01, additional images were taken with an optical microscope in order to resolve smaller features.

Image Analyses

In order to characterize the textures of the olivine aggregates' we manually traced the grain boundaries, Fe-Ni pockets, troilite pockets, and fractures using the commercial program Adobe Illustrator (Fig. 2). Fe-Ni and troilite (FeS) textures were easy to trace based on their bright color compared to the dark green-brownish color of the olivines (e.g., Fig. 1). In this study, we do not distinguish between Fe-Ni and troilite as they have either been present as a single melt phase at high temperature or, if immiscible, they would have acted structurally similar (see discussion on troilite distribution in Walte et al., 2020). By extension of the argument, minor amounts of chromite filling primary or secondary features in the olivine aggregates were also not distinguished in Fig. 2 and included in the analyses, because these features are texturally similar and continuous with the other two opaque phases. In most cases, grain boundaries were also well recognizable within olivine aggregates; however, in some cases, the boundaries were blurry, weakly defined, or obscured, for example by secondary weathering. Such regions were either excluded from grain-size analyses or, if possible, the location of ambiguous grain boundaries and triple junctions was inferred indirectly. The effect of possible tracing errors is expected to be small due to the generally good resolution of grain boundaries. Furthermore, any remaining systematic bias is expected to be similar for all samples, as all tracing and textural

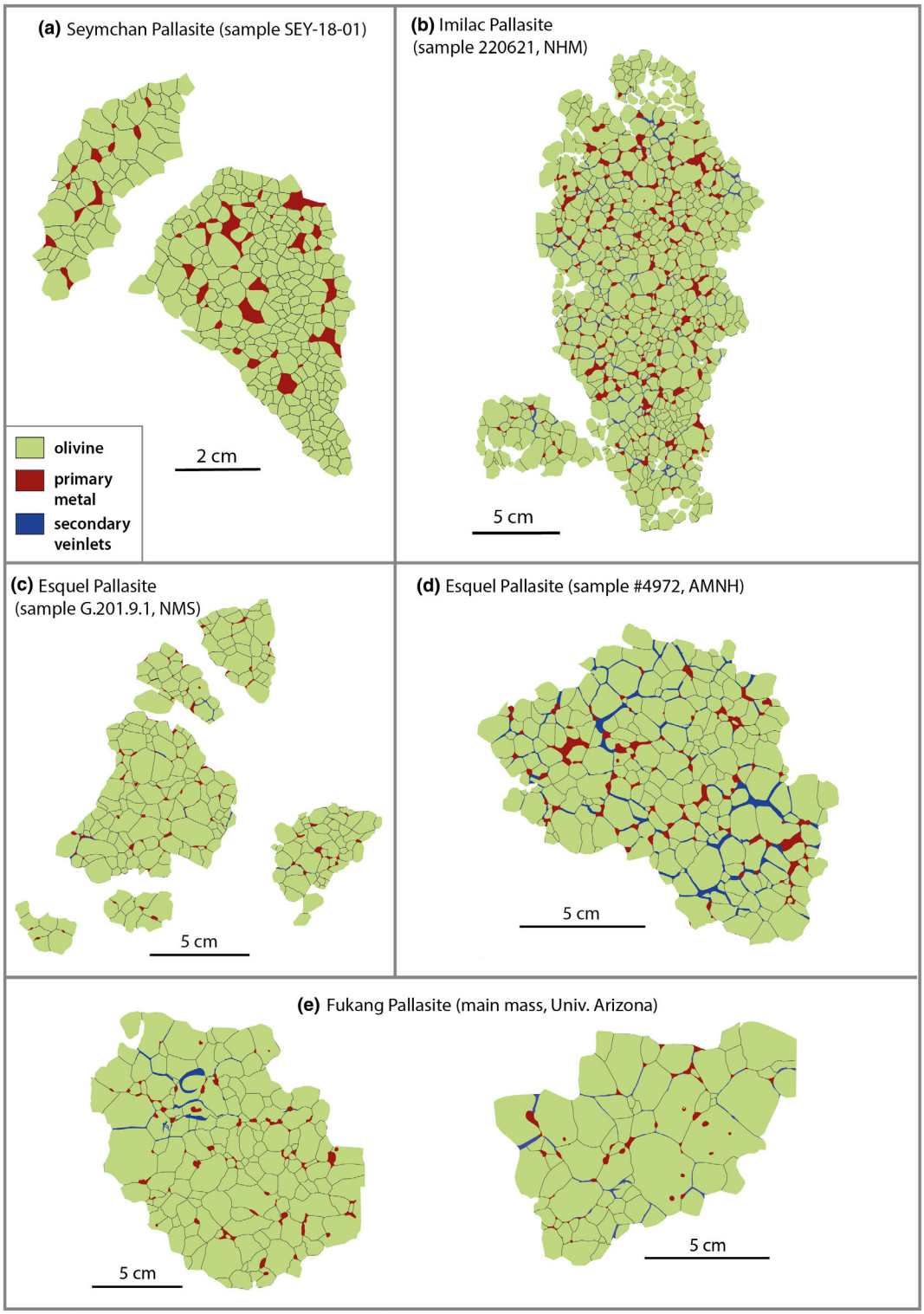

Fig. 2. Textural interpretation of olivine aggregates of Seymchan, Imilac, Esquel, and Fukang pallasites indicating olivine grains (green), primary metal pockets (red), and secondary veinlets and fractures (blue). Note the different grain sizes and the differences in primary metal fraction. See all figures in the supporting information for photographs of the olivine aggregates and overview images marking the locations of analyzed olivine aggregates. a) Seymchan pallasite (sample SEY-18-01). b) Imilac pallasite (sample 220621, NHM). c) Esquel pallasite (sample G.2010.9.1, NMS). d) Esquel pallasite (sample #4972, AMNH). e) Fukang pallasite (main mass, Univ. Arizona). (Color figure can be viewed at wileyonlinelibrary.com.)

interpretation was performed by the first author. The resulting drawings were converted into binary format and exported into the public domain software ImageJ (National Institutes of Health, USA) for further analyses. The software was used to analyze automatically the sizes of each olivine grain and primary metal pocket (diameter of area equivalent circles). The grain-size distributions of the pallasites were normalized as described, for example, in Faul and Scott (2006). For this purpose, the individual grain-size measurements were normalized by the average grain size measured in the olivine aggregates of the respective pallasite; subsequently, the data were binned with a bin-width 0.2 times the average grain size. The frequency of the bins was determined by normalizing the bin count with the number of measurements contained in the largest bin. This normalization procedure allows for a better comparison of grain-size distributions between different pallasites with varying average grain sizes and population numbers. All reported data were derived from 2-D sections of originally 3-D olivine aggregates, which is unavoidable considering the size and shape of the available sample slices. While the true volume fraction of a phase (e.g., of metal pockets) is equal to the area fraction measured for a section given a large enough sample size, the true 3-D grain size and especially the grain-size distribution of a polycrystalline aggregate differs non-trivially from the values determined from a 2-D section (e.g., German, 2010). We only corrected for this effect when reporting the average grain size and the average metal pocket size, which is determined from the average diameter in 2-D by multiplying by a factor of 1.27 (Kong et al., 2005) to be compatible with previously published literature on grain size in pallasites (Solferino & Golabek, 2018; Solferino et al., 2015). The error bars given in the analyses below reflect the variation of grain sizes and metal fractions measured between different pallasite samples and/or between different olivine aggregates within a single pallasite slice, being significantly larger than errors from the measurement procedure described above.

Laboratory Deformation Experiments

In order to identify and better understand the textural overprints caused by the pallasite formation event found in the different olivine aggregates, we compared the textures to microstructures found in two deformation experiments that were performed with the SAPHiR three-axis multianvil press as part of a previous study (Walte et al., 2020). The cubic multianvil press is identical to the previously described Mavo press located at BGI, University of Bayreuth, Germany (Manthilake et al., 2012), and allows for controlled deformation at high strain rates $>1 \times 10^{-3}$ s^{-1} relevant for pallasite formation (Walte et al., 2020). The aim of the laboratory experiments was to simulate a static annealing stage in a dunitic mantle containing a small fraction of metal melt (the primary metal pockets) that was followed by an episode of fast deformation and intrusion of external metal melt and either quenching or postdeformation static annealing at high temperature.

Following a brief description of the experiments (samples 177 and 178 in table 1 and methods section 2 in Walte et al., 2020), both experiments employed a 3×3 mm sized sample capsule containing San Carlos olivine powder that was mechanically mixed with 10 wt% of FeS. A cavity at the center of the sample contained a small volume of gold that simulated external metal melt as it intruded into the adjacent olivine–FeS matrix during deformation. The FeS and Au model system is largely immiscible thereby allowing us to distinguish between melt pockets already present in the olivine matrix (FeS) before deformation and newly "intruded" metal melt (Au) derived from a separate source (the cavity). Despite differences between the Au–FeS model system and Fe-Ni-S melts with regard to melting temperatures and surface energies, the behavior during high strain rate deformation and annealing is qualitatively similar (Walte et al., 2020). The samples were cold compressed to 1 GPa and subsequently heated to 1350 °C, well above the FeS and Au liquidus, and statically annealed for 22.5 h. After annealing, the temperature was lowered to 1300 °C and both samples were deformed by axial compression at a strain rate of approximately 5×10^{-3} s^{-1} with a total deformation duration of only ≈20 s. After deformation, the first sample (SA 177) was quenched within seconds by switching off the electrical heating supply, whereas the second sample (SA 178) was statically annealed for 2 h at a temperature of approximately 1300 °C. Polished central sections of the samples were analyzed and photographed by optical microscopy.

RESULTS

Petrographic Criteria for Primary and Secondary Metal Textures

According to the principles laid out in the introduction of this article and in Walte et al. (2020), primary metal pockets were identified as (i) round metal inclusions inside olivine grains, whose diameter is larger than the width of adjacent veinlets (typically millimeter scale) and that do not lie aligned with other metal inclusions or veinlets; (ii) equiaxed metal pockets at olivine triple or quadruple junctions and smooth, often convex outward curving grain boundaries; and (iii) larger, often irregular metal pockets that are bordered by

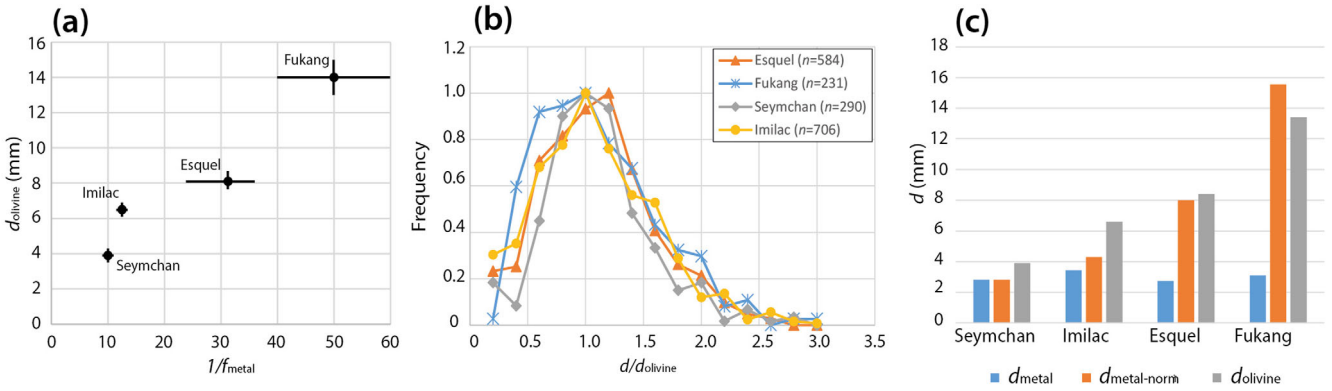

Fig. 3. Grain size and primary metal fraction in pallasites. a) Average grain size versus inverse primary metal fraction in olivine aggregates. The relation may indicate Zener pinning inhibited grain growth in the PPB. b) Normalized grain-size distributions are self-similar indicating a common grain growth mechanism. c) Primary metal pocket size d_{metal} and normalized metal pocket size $d_{metal\text{-}norm} = d_{metal}/(f_{metal}/f_{metal\text{-}Seymchan})$ compared to the olivine grain size $d_{olivine}$. (Color figure can be viewed at wileyonlinelibrary.com.)

more than four olivine grains. The olivine grains display smoothly curved phase boundaries in contact with the metal indicating local surface energy minimization (Scott, 1977) as opposed to straight surfaces resembling former grain boundaries or fractures.

Secondary features are identified as elongated metal-filled fractures and veinlets either along former olivine grain boundaries (intergranular fractures, cf. Scott, 1977) or cross-cutting olivine grains (intragranular fractures, cf. Scott, 1977). For wider metal-filled veinlets, for example, at the fringes of the olivine aggregates, the criterion is that adjacent olivine grains are angular and geometrically fit like a jigsaw puzzle as opposed to large primary metal pockets that are bounded by olivines with rounded phase boundaries (case [iii] above). In places where primary metal pockets are interconnected by secondary veinlets, the separation of the two features was clear in Seymchan and Imilac and more diffuse in Fukang and Esquel leading to some ambiguity as described below. Based on these criteria, olivine aggregates of Fukang, Seymchan, Imilac, and Esquel were redrawn and interpreted forming the basis of the following analyses (see Fig. 2 for examples).

Olivine Grain Sizes and Primary Metal Fraction in Olivine Aggregates

The analyzed average olivine grain size and the volume fraction of primary metal pockets (also interpreted as the primary metal fraction in the following) for all samples is provided in Table 1. The average grain sizes $d_{olivine}$ and the primary metal fraction f_{metal} vary considerably between the different pallasites with Seymchan displaying the smallest olivine grains ($d_{olivine} \approx 4$ mm) and largest primary metal fraction ($f_{metal} \approx 0.10$), whereas Fukang displays the largest olivine grains ($d_{olivine} \approx 14$ mm) and smallest metal content ($f_{metal} \approx 0.02$) (Table 1; Fig. 2). In fact, the olivine aggregates in all four pallasites display a roughly inverse relation between average olivine grain size and primary metal fraction (Fig. 3a), which may suggest a causal relation as discussed below. Despite the different absolute grain sizes, the normalized grain-size distribution diagrams for the four pallasites are self-similar (Fig. 3b) indicating textural equilibrium and a common grain-growth mechanism for all aggregates (e.g., Faul & Scott, 2006; German, 2010) with a maximum frequency falling onto the average grain size and the largest grains being approximately three times larger than the average grain size. The olivine grain boundaries are generally smoothly curved and metal-free olivine triple junctions display frequent 120° angles in all olivine aggregates confirming textural equilibration and surface energy-driven grain growth.

Olivine–Metal Textures in Olivine Aggregates

Primary Metal Pockets

Primary metal pockets that are surrounded by olivines and not interconnected by veinlets or fractures in the exposed sections were found in all investigated olivine aggregates (Fig. 4). Relatively small metal pockets are equiaxed and display a high dihedral angle >60° and convex boundaries toward the olivine when situated in triple junctions (Figs. 4b and 4c). Larger metal pockets bordering more than four grains are more irregular including smoothly rounded grain boundaries observed in protruding olivine grains (Figs. 4a and 4d) as discussed in Walte et al. (2020). In contrast to the grain size that varies by a factor of three between the different pallasites, the average size of primary metal pockets d_{metal} remains similar

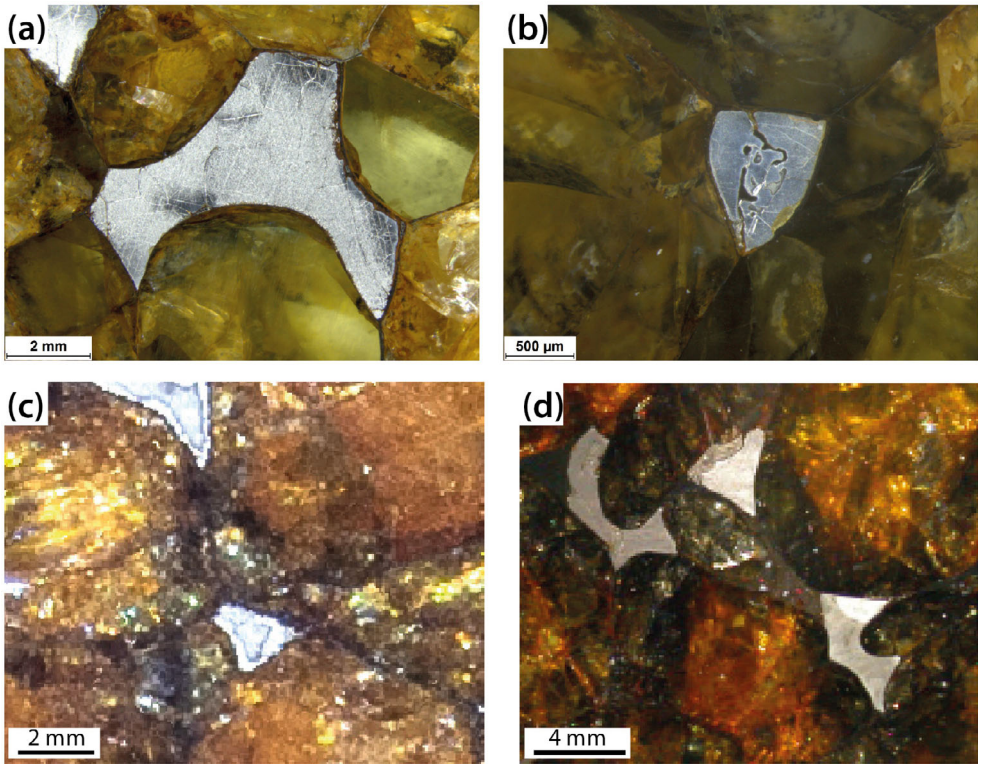

Fig. 4. Primary metal pockets found in undisturbed parts of the olivine aggregates. The shape is determined by the high dihedral angle of Fe-Ni metal with olivine and ongoing grain growth. a, b) Seymchan pallasite SEY-18-01. c) Esquel pallasite #4958 (Credit: Denis Finnin, AMNH). d) Fukang pallasite (Credit: Dolores Hill, Univ. Arizona, Lunar & Planetary Laboratory). (Color figure can be viewed at wileyonlinelibrary.com.)

(Fig. 3c; Table 1). However, taking the different metal fractions into account, achieved by normalizing to the primary metal fraction of Seymchan $d_{\text{metal-norm}} = d_{\text{metal}}/(f_{\text{metal}}/f_{\text{metal-Seymchan}})$, a correlation between normalized metal pocket size $d_{\text{metal-norm}}$ and the average grain size can be observed (Fig. 3c). This may indicate simultaneous growth of metal pockets and olivine grains as is commonly found in two-phase grain-growth experiments (Hiraga et al., 2010).

Fractures and Veinlets

Secondary textures in the form of metal-filled veinlets and fractures are also present in olivine aggregates of all four pallasites (Figs. 5–6); however, their shape and appearance differ among the investigated pallasites. In Seymchan and Imilac, the distinction of primary and secondary metal textures is pronounced as described in the Introduction section. Veinlets generally have a brittle appearance, they often follow along grain boundaries (intergranular fractures), and also display sharp transitions to the adjacent olivines (Figs. 5a and 6a–d). They are generally continuous with no signs of pinch-off and can be narrower than 20 µm (Seymchan, Fig. 5a) or 100 µm (Imilac, approaching the resolution of the available optical images). When cutting through primary metal pockets, the outer shape of the latter is retained in Seymchan and Imilac aside from being pulled apart by extension, which creates sharp olivine nooks at the former olivine–olivine–metal triple junctions in Seymchan (Fig. 6a). In Imilac, these nooks are locally slightly rounded (Figs. 6c and 6d). In Esquel and especially in Fukang, however, veinlets display a smoother appearance that is created by locally rounded olivine edges, varying widths, and blunted veinlet tips (Figs. 6e–h). Narrower veinlets are sometimes locally pinched-off resulting in aligned elongated metal melt lenses (Figs. 5b and 6h). Unlike in Seymchan and Imilac, the interaction of secondary veinlets with primary metal pockets does not appear to preserve the shape of the latter in Fukang and Esquel, but changes their outline at triple junctions from convex to concave and apparently reduces their size (Figs. 6e–h). While the aforementioned "blending" of primary and secondary olivine–metal features is the rule in Fukang, Esquel additionally displays intermediate textures where the primary pocket outlines are still visible, but the olivine nooks at the former triple junctions are more smoothly rounded than in Imilac (Fig. 6e). In summary, the resulting order from sharp-brittle to smooth-blunted olivine–metal textures is Seymchan, Imilac, Esquel, and Fukang.

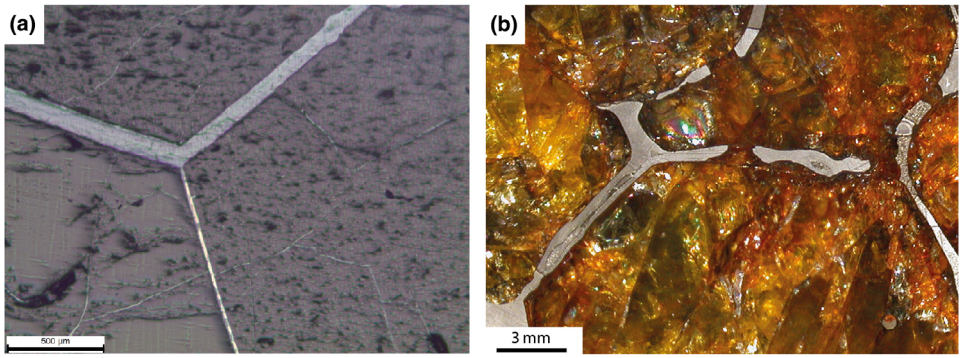

Fig. 5. a) Optical microscope image of thin intergranular fractures filled with Fe-Ni or troilite in Seymchan that show no sign of pinch-off. Also note the even thinner intragranular fractures. b) Pinched-off veinlet in Fukang indicates beginning re-equilibration after formation and hence slower cooling than Seymchan (Credit: Dolores Hill, Univ. Arizona, Lunar & Planetary Laboratory). (Color figure can be viewed at wileyonlinelibrary.com.)

Experiments

In order to simulate the difference in olivine–metal textures between the pallasites that was described above, the role of postdeformation annealing was explored experimentally. Figure 7 shows the difference between an immediately quenched sample and a sample that was annealed at high temperature for 2 h after both samples were deformed at similar high strain rates in the brittle deformation regime. The immediately quenched microstructures reveal a preservation of the outer shape of "primary" metal pockets (i.e., FeS pockets that were statically equilibrated in the olivine matrix before deformation) where they are cut by intergranular fractures (Fig. 7a). These features are similar to the textures in Seymchan and Imilac (Figs. 6a–d). On the other hand, in the postdeformation annealing experiment, the intergranular fractures have a smoother appearance similar to the textures found in Fukang and Esquel aggregates (Fig. 5b, Figs. 6e–h) including local pinch-off into isolated lenses. In this experiment, the FeS–olivine boundaries at interconnected triple junctions likewise locally display a concave curvature (Fig. 7b). Hence, these textural differences are caused by high-temperature annealing after deformation (event [3] of Scott, 1977, see the Introduction section in this article) and not by differences during the deformation stage (event [1-2] of Scott, 1977). This also explains the differences in olivine–metal textures between the pallasites described above. Another observation from the experiments is that in olivine aggregates, primary metal pockets and secondary veinlets are not necessarily filled with primary metal melt and newly intruded metal melt, respectively. In the experiments, both microstructures can contain either remobilized primary metal or secondary metal melt (FeS and Au melt from the collapsed central cavity, respectively) as long as they are connected to the outside olivine–metal mush (Fig. 7a). In pallasites, this may contaminate the trace element and isotopic signature of apparently primary metal pockets.

Evidence for (Partially) Molten Primary Metal Pockets

Experimental studies have shown that significant static grain growth in olivine–Fe-S aggregates on geologically viable time scales requires at least partially molten Fe-S pockets (Solferino & Golabek, 2018; Solferino et al., 2015), which applies to the development of the large olivine grain sizes observed in pallasites. Likewise, the interplay between the primary metal pockets and the secondary textures described in the previous sections requires that both were still (partially) molten during the deformation that formed the pallasites and for some time after the event in case of Fukang and Esquel. Figure 8 shows several textural details found in Seymchan, Imilac, and Esquel that support these conclusions. Here, large primary metal pockets contain small olivine fragments and partially rounded olivine grains. The size and especially the elongated shape of the small olivines indicates that they were formed by deformation during the pallasite formation event. In order to enter the metal pockets, the metal must have been liquid. This combined evidence indicates that the pallasite-forming event deformed a warm mantle featuring solid olivines and largely molten primary metal pockets.

DISCUSSION

Evolution of Olivine–Metal Textures Recorded in the Olivine Aggregates

Our results confirm the presence of two distinct metal textures, namely primary metal pockets and secondary veinlets, in all investigated olivine aggregates

of MG pallasites. This observation is compatible with a shared geological history in the mantle of a common PPB and reveals that the PPB underwent a complex multistage history as discussed below. While isolated primary metal pockets have a similar appearance in all pallasites that is determined by local surface energy minimization in agreement with experimental work and theoretical considerations (Minarik et al., 1996; Walte et al., 2007), the secondary features and their interplay with primary metal pockets vary between the investigated pallasites. We observed a postdeformation alteration of secondary veinlets in Esquel and Fukang characterized by local pinch-off and tip-blunting that was largely absent in Imilac and especially Seymchan (Figs. 5 and 6). Additionally, a different interplay between primary metal pockets and secondary veinlets was seen in Seymchan and Imilac on the one hand and Esquel and Fukang on the other that was reproduced by our experiments. While the texture of the first group can be understood by simply pulling the olivine aggregates apart and filling the former grain boundaries with metal, the second group displays a clear postdeformation alteration of these metal–olivine textures (event [1]–[2] and event [3], respectively, after Scott, 1977). Considering the high surface energy of metal melt with olivine, the elongated metal pocket and triple junction shapes in the latter group are also not equilibrated; however, their formation and relevance for pallasite evolution can be understood when considering local crystal–liquid annealing processes. Previous in situ experimental studies in crystal–liquid analogue systems revealed that liquid pockets temporally assume smooth but elongated disequilibrium shapes while re-equilibrating from textural disturbances, which may also include a temporary change in crystal–liquid curvature (Walte et al., 2003, 2007). In the olivine aggregates and the experiments, the cause of the disturbance was the creation of intergranular fractures by deformation. Hence, the four pallasites (1) Seymchan (pristine deformation textures), (2) Imilac (start rounding of sharp olivine corners and nooks), (3) Esquel (local pinch-off and blunting of veinlets, rounded nooks, and blending of primary and secondary textures), and (4) Fukang (local pinch-off and blunting of veinlets, blending of primary and secondary textures, change of metal–olivine curvature from convex to concave) can be interpreted to preserve a time series of beginning textural re-equilibration. Based on these inferences, a schematic evolution of the metal textures in olivine aggregates is reconstructed (Fig. 9) that can be connected to the three events of Scott (1977) and the large-scale evolution of the MG PPB: predeformation grain growth preserved in central parts of all olivine aggregates (Fig. 9a, "event [0]"), deformation by the pallasite formation event best preserved in Seymchan and Imilac aggregates (Fig. 9b, events [1]–[2]), and beginning of postdeformation annealing as recorded by Esquel and Fukang (Fig. 9c, event [3] of Scott, 1977). The final step of full re-equilibration of olivine–metal microstructures would result in a texture indistinguishable from the initial stage (Fig. 9a). Unfortunately, the limited number of experiments and the use of FeS melt in contrast to the Fe-Ni-S melt in pallasites do not allow for a kinetic scaling of the early annealing processes from the experiments to nature at this stage. Hence, we can only refer to the earlier conclusion that Seymchan must have cooled rapidly below the Fe-Ni-S solidus (≈980 °C) within several months to years that was based on scaling of experimentally determined rounding kinetics of small olivine grains (Walte et al., 2020). The preservation of intergranular metal veinlets with a width of less than 20 μm without signs of pinch-off (Fig. 5a) is also a strong indication of rapid cooling of Seymchan. We can add that our new textural observations indicate slower cooling of the other pallasites in the order given above. One possible interpretation is that the cooling order reflects burial depth after the pallasite formation event with Seymchan being closest to the surface, and Imilac, Esquel, and Fukang successively located at greater depth. This inference is largely supported by the subsequent, much slower, cooling history determined from metallographic cooling rates in the temperature range between approximately 700 and 400 °C (Yang et al., 2010). A cooling rate of 7.1 K Myr^{-1} was determined for Seymchan based on the Ni diffusion profile in taenite lamellae of Widmanstätten patterns, and Imilac and Esquel yield averaged cooling rates of approximately 4 and 3.3 K Myr^{-1}, respectively, based on the cloudy zone particle sizes and the tetrataenite bandwidths (Yang et al., 2010) thus reflecting our order at a high temperature of >980 °C. For Fukang, a cooling rate of 5.8 K Myr^{-1} can be calculated based on cloudy zone particle size, slower than Seymchan, but faster than Imilac and Esquel that seems to contradict the cooling order we inferred from textures. However, only 15 particles were measured in Fukang as opposed to 23–133 particles for the other pallasites and no values for tetrataenite widths were determined for Fukang (table 1 in Yang et al., 2010). This results in a greater uncertainty of the cooling rate compared to those of the three other pallasites. On the other hand, a deep burial of Fukang is suggested by petrologic investigations resulting in a pressure bracket between ≈0.30 GPa and <0.4 GPa based on two-pyroxene barometry and the stability of tridymite inclusions, respectively (DellaGiustina et al., 2019). While the deepest burial of Fukang confirms our textural

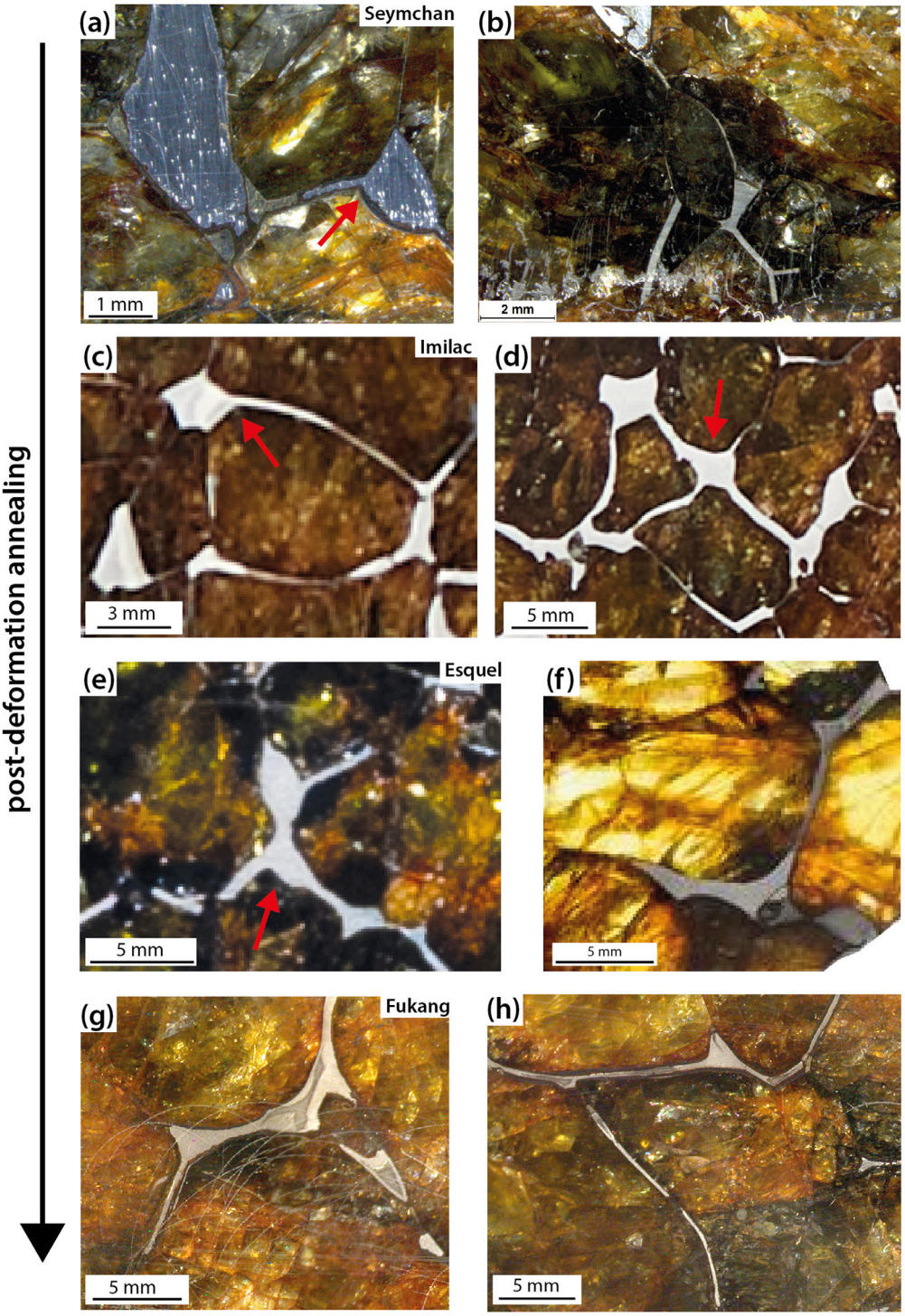

Fig. 6. Intergranular fractures and veinlets (secondary features) and their interplay with primary metal pockets in olivine aggregates. a, b) Seymchan SEY-18-01. c, d) Imilac (© The Trustees of the National History Museum, London). e) Esquel #4958 (Credit: Denis Finnin, AMNH). f) Esquel G.2010.9.1 (© National Museums Scotland, Edinburgh). g, h) Fukang (Credit: Dolores Hill, Univ. Arizona, Lunar & Planetary Laboratory). a–d) Primary pockets that are cut by veinlets are well preserved in Seymchan and Imilac, although the nooks are sharp in Seymchan and slightly rounded in Imilac (red arrows). e, f) In Esquel, the distinction between primary metal pockets and veinlets is often partially blurred (red arrow) or primary metal pockets and veinlets merge to new shapes with concave curvature as is the rule in Fukang. g, h) In Fukang, intergranular veinlets display pinch-off and blunted tips also indicating annealing. These textures indicate an increase in postdeformation annealing from Seymchan to Fukang as indicated by the side arrow (see also Fig. 7). (Color figure can be viewed at wileyonlinelibrary.com.)

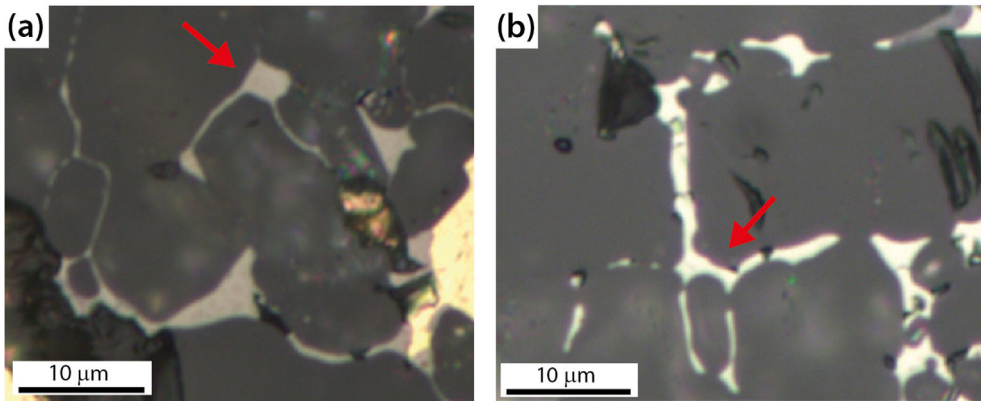

Fig. 7. Central parts of synthetic olivine aggregates obtained from deformation experiments illustrating the interplay between "primary" FeS pockets and secondary intergranular veinlets. a) Primary FeS pockets (red arrow) retain their shape when cut by veinlets in the sample that was immediately quenched after deformation. b) No clear distinction between primary and secondary features after 2 h postdeformation annealing. Note a predominance of concave FeS–olivine contacts in triple junctions (red arrow). The experiments qualitatively reproduce the differences between Imilac/Seymchan and Esquel/Fukang shown in Fig. 6. (Color figure can be viewed at wileyonlinelibrary.com.)

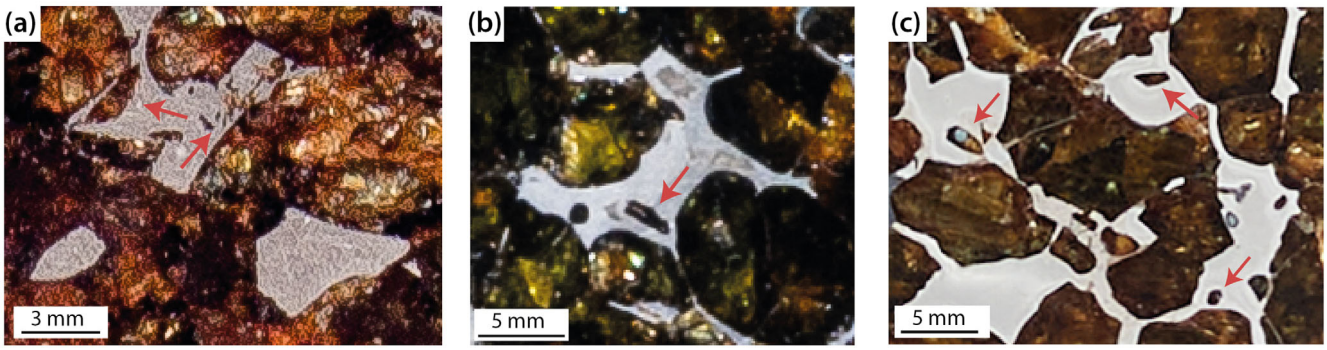

Fig. 8. Details of olivine aggregates that show small olivine fragments inside large broken-up primary metal pockets (red arrows). The olivine fragments could only have entered the metal pockets if they were molten during the deformation. a) Seymchan #5168 (Credit: Denton Ebel, AMNH). b) Esquel #4958 (Credit: Denis Finnin, AMNH). c) Imilac (© The Trustees of the National History Museum, London). (Color figure can be viewed at wileyonlinelibrary.com.)

observations, whether a depth of >200 km (DellaGiustina et al., 2019) is compatible with the only partial re-equilibration of the metal–olivine textures and recent suggestions of a thin mantle of the MG PPB (Nichols et al., 2021) remains to be investigated.

Grain Growth in the Dunitic Mantle and the Cause of Grain-Size Variations in Pallasites

The large size of the olivine grains, hence often called by their gem name peridot, is a common property of all pallasites adding to their perceived visual attraction and sparking scientific curiosity for more than 200 yrs. In general, grain-size analyses of pallasites were complicated by the difficulty in discerning among intact olivines, olivine fragments, and small aggregates that are all found embedded in the Fe-Ni matrix of pallasites. Our approach of tracing grain boundaries in the olivine aggregates removes this uncertainty and ensures that the resulting grain size reflects the property of the host rocks. Solferino et al. (2015) reported grain-size measurements for Seymchan and the round-olivine type pallasites Brenham and Springwater. The average grain size reported for Seymchan (3.9 mm) is identical to our results and the grain-size distributions are similar. This shows that our two approaches are compatible and that their data on the two round type pallasites can be taken into account for further discussion.

Despite Seymchan yielding the lowest grain size of the investigated pallasites, its average grain size of ≈4 mm is still more than an order of magnitude larger than its likely chondritic precursor material, thereby suggesting an important role of static grain growth

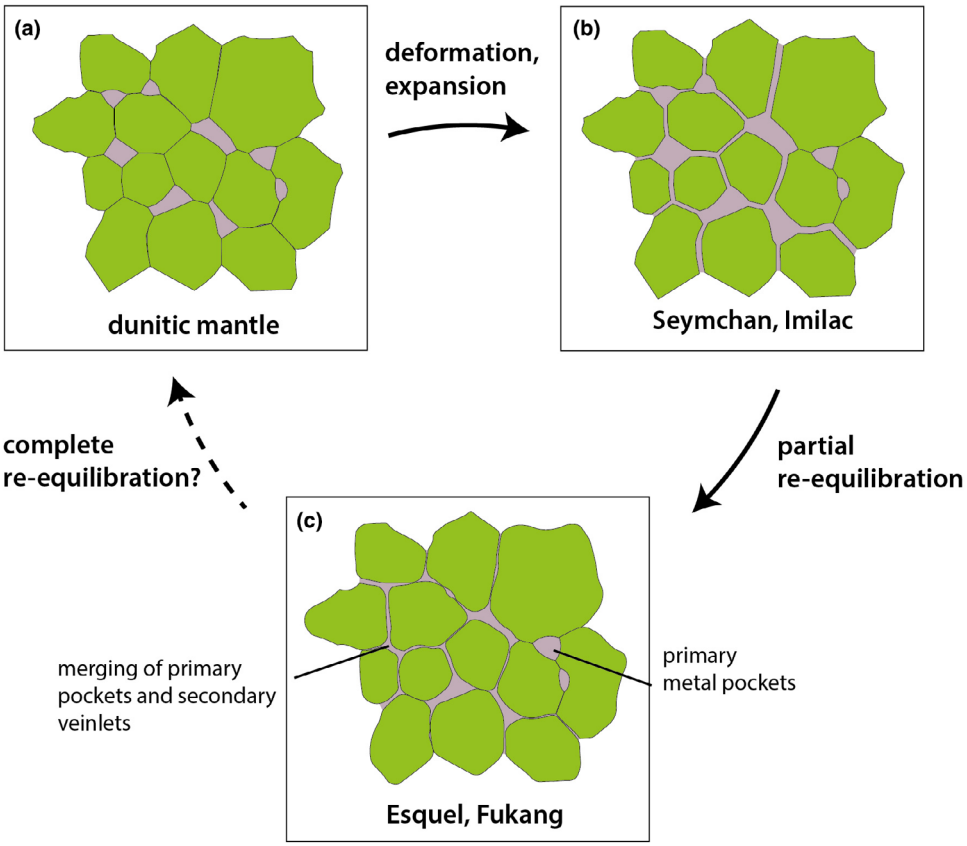

Fig. 9. Schematic textural evolution of the olivine–metal textures during and after the pallasite formation event. a) Dunitic part of the mantle with primary metal pockets as preserved in undisturbed parts of olivine aggregates. b) Pallasite formation creates fractures that interconnect primary metal pockets. This stage is preserved in Seymchan and Imilac. c) Beginning of postdeformation annealing causes merging of primary and secondary textures. Note that *isolated* primary metal pockets are not altered at this stage, as they are already equilibrated. Further hypothetical annealing would re-establish full textural equilibrium. (Color figure can be viewed at wileyonlinelibrary.com.)

inside the MG PPB (Solferino & Golabek, 2018; Solferino et al., 2015). Our measurements reveal an approximately inverse correlation of grain size to the fraction of primary metal (Fig. 3a). Despite the low sample number ($n = 4$) compared to the currently known total number of 48 MG pallasites (Meteoritical Bulletin website), to our knowledge, these pallasites contain the best examples of olivine aggregates with a sufficient size that is the prerequisite for the performed analysis. Hence, in the following discussion, we will make the preliminary assumption that this relation is both representative and causal for both angular and fragmental MG pallasites.

Scott (2017) suggested that olivine aggregates may form from Brenham-like source rocks initially containing a high metal-melt fraction (approximately 30 vol%) that lose various amounts of metal-melt during compaction and simultaneous grain growth. According to this hypothesis, the different pallasites would represent different parts of a PPB mantle whose textures were arrested at different times preserving different stages of this melt-loss grain-growth continuum. In material science, such a coupled process is known as liquid-phase sintering (German, 2010), which produces a roughly linear grain size versus inverse melt fraction evolution over time (German, 2010) similar to those found here. However, this hypothesis is ruled out by the on average larger grain size of round-type pallasites such as Brenham and Springwater compared to Seymchan (5–6 mm and ≈4 mm, respectively; Solferino et al., 2015). Hence, the process suggested by Scott (2017) would indicate first a grain-size *decrease* from Brenham to Seymchan, followed by an *increase* during ongoing primary metal melt loss to form the other olivine aggregates. This is incompatible with liquid-phase sintering theory. Furthermore, a possible primary metal melt loss below the metal fraction found in Seymchan aggregates is hindered by the low mobility of high dihedral angle melts as the system approaches textural equilibrium. Energetic considerations (Walte et al., 2007) and

experimental studies (Bagdassarov et al., 2009; Néri et al., 2020; Solferino et al., 2020) showed a connectivity threshold in the range of 10–15 vol%, incidentally the highest primary metal fraction found so far in olivine aggregates (Seymchan—Walte et al., 2020). It is difficult to pinpoint when this equilibrium and pinch-off is achieved during annealing, but a twofold grain-size increase should be sufficient, which was reached during an early stage considering a grain-size increase over one to two orders of magnitude while transforming chondritic to pallasite textures.

A better explanation for the observed relation between grain size and primary metal fraction is contemporaneous olivine grain growth in different mantle regions characterized by different, but constant, fractions of metal melt. Here, the minor phase (primary metal melt) slows down grain boundary migration in the major phase (olivine) by Zener pinning (Smith, 1948), whose effect increases with volume fraction of the minor phase. Experimental studies explored the pinning effect of Fe-S melt pockets on olivine grain growth and obtained an inverse relationship between olivine grain size and Fe-S metal melt fraction (Solferino & Golabek, 2018; Solferino et al., 2015), which is compatible with our observations. For the MG PPB, the grain growth episode would have started after (partial) differentiation and was terminated by the pallasite-forming event. Unfortunately, the olivine–Fe-S melt grain growth data of Solferino and Golabek (2018) do not consider Fe-S melt fractions below 10 vol% and the uncertainties of the resulting grain growth equation coupled with the temperature uncertainty result in a duration between <0.5 and more than 100 Myr to reach the grain size of Seymchan pallasite. However, considering that the primary metal pockets were still largely molten when the pallasite formation event occurred, as argued based on our textural observations, we suggest that the duration of the grain growth episode was likely toward the lower end of the estimation.

In summary, we argue that the variation of primary metal observed in olivine aggregates reflects mantle heterogeneities that were formed during or shortly after core–mantle differentiation and that controlled the subsequent grain growth process experienced by their different source regions. The higher average grain size of round type pallasites reported by Solferino et al. (2015) is not explained by the Zener pinning mechanism and their place in the PPB evolution remains open for further inquiry.

Origin and Distribution of Primary Metal in the Mantle of the MG PPB

Closely related to the origin of the primary metal is the question of lateral distribution in the mantle. Most previous pallasite formation models do not consider separate generations of metal melt. However, a depth stratification of increasing primary metal fraction toward the core–mantle boundary would be best compatible with the pallasite formation model of Boesenberg et al. (2012) that suggests pallasite formation at the core–mantle boundary during differentiation and the metal melt-loss model of Scott (2017) discussed above, while the two-stage model of Walte et al. (2020) postulates a non-gradual, heterogeneous distribution of primary metal throughout the dunitic parts of the mantle that is stranded as a result of only partial differentiation (Fig. 10a).

Arguments for a non-regular and heterogeneous distribution of primary metal are supported by a heterogeneous primary metal content inside single pallasites. For example, recent investigations in Brahin reported both round olivine textures and angular and fragmental olivine textures (McKibbin et al., 2019). Round olivines imply an elevated primary metal content to form the smoothly curved boundaries, whereas angular and fragmental olivines indicate former dry grain boundaries suggesting a low to moderate primary metal content. We made similar observations in unpublished images of the Sericho pallasite, where metal-poor olivine aggregates are situated adjacent to aggregates with a large primary metal fraction. This shows that the fraction of primary metal was strongly heterogeneous even on the decimeter length scale in some pallasites, thereby questioning any regular large-scale gradation.

Our results suggest a postdeformation burial depth of the pallasites that coincides with a *decrease* in primary metal fraction from Seymchan to Fukang. If true and if this ordering also reflects a predeformation depth profile, the MG PPB mantle may have been characterized by an inverse depth stratification. Such a decrease in metal fraction from surface to depth is incompatible with gravitational differentiation processes and could only be the result of postdifferentiation metal intrusion, for example, by a complex collisional history of the PPB. According to this hypothesis, earlier impactors would have delivered metal melt to the upper to middle PPB mantle whose textural history would have been obliterated by static annealing as shown in Figs. 9c to 9a, before the final pallasite-forming impact took place (Fig. 10b). In order to form the inverse correlation between olivine grain size and primary metal fraction discussed in the previous section, the impacts must have delivered the metal early after PPB formation; before the static grain growth stage and while internal radiogenic heating was still active. Retaining such an early inverse metal stratification during grain growth further requires a non-convecting PPB mantle as proposed in the next section.

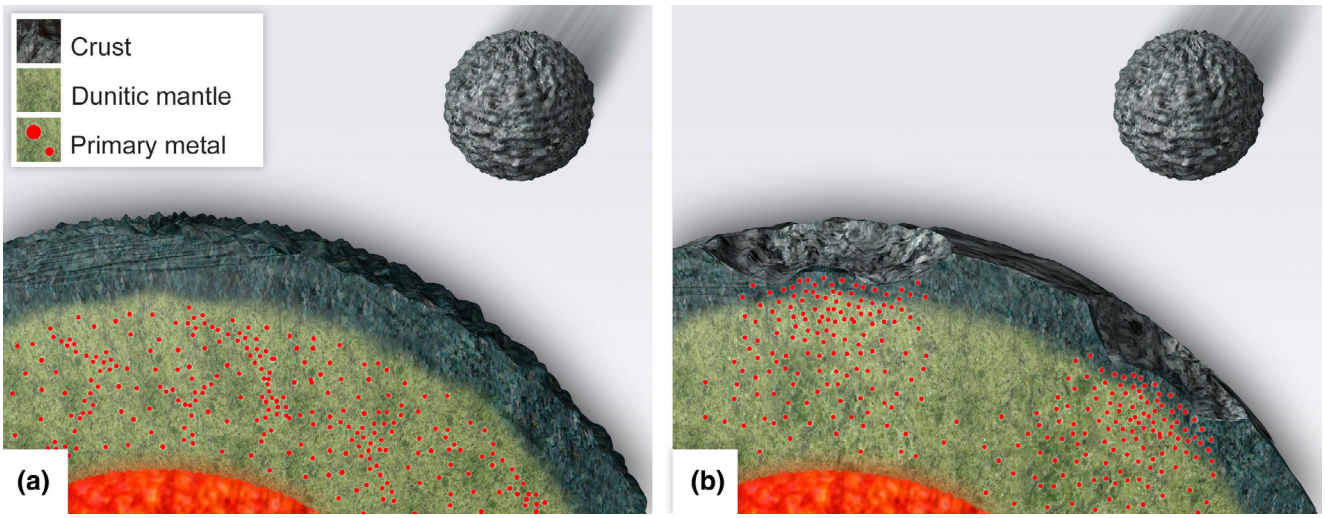

Fig. 10. Schematic illustration of hypotheses for distribution and origin of primary metal pockets in the PPB mantle before the final two-body collision that formed the pallasites. a) Heterogeneous but non-gradational distribution of stranded metal pockets after partial differentiation (after Walte et al., 2020). b) Inverse gradation of primary metal fraction as a result of an earlier impact history. The impacts must have hit early after differentiation in order to allow full textural annealing by ongoing ^{26}Al decay heating. Credit: Reiner Müller, FRM II/TU Munich. (Color figure can be viewed at wileyonlinelibrary.com.)

Preimpact Dynamics of the MG PPB Mantle

As argued above, primary metal pockets were likely to be at least partially molten throughout the early history of the studied MG PPB until the pallasite formation event. This allows us to use the shape of primary metal pockets as a marker for the prepallasite dynamics of the mantle. During deformation, an olivine–metal melt system is determined by its strongly contrasting viscosity between the two phases and by the high surface tension of the melt pockets. While deformation tends to localize into the lower viscosity phase (the metal melt) thereby elongating melt pockets along the shear direction, surface tension counteracts elongation by aiming to retain a spherical shape (Kohlstedt & Holtzman, 2009; Llorens et al., 2019; Walte et al., 2011). The balance of these effects depends on the flow stress and the inverse of the metal melt pocket size, defining a stress-dominated and a surface tension–dominated deformation regime (Walte et al., 2011). The largely equiaxed primary metal pockets and the absence of any systematic elongation place olivine aggregates in the latter field, which indicates maximum strain rates of $\approx 1 \times 10^{-15}$ s^{-1} for a metal pocket size of several millimeters. This means that the dunitic parts of the MG PPB mantle were essentially non-convecting.

We calculate for different core radius and planetesimal radius combinations the bottom Rayleigh number to estimate under which conditions the minimum critical Rayleigh number necessary for the onset of solid-state convection in a bottom-heated system is not reached (Turcotte & Schubert, 2014). Unlike in the scenario of Solferino and Golabek (2018), we assume that all silicate melts with low melting temperatures like feldspars (hosting ^{26}Al) and pyroxenes migrated toward the surface after their melting temperature was reached (Lichtenberg et al., 2019). Thus, olivine is considered to be the only remaining solid silicate in the MG PPB mantle. We employ for the MG PPB mantle a dry olivine rheology (Karato & Wu, 1993) with limited rheological weakening due to the presence of metallic melt (Hustoft et al., 2007). To test different ideas for the MG PPB interior structure, we vary the core radius between 10 and 250 km, while the MG PPB radius can reach up to 360 km. Only planetesimals with >340 km radius overstep the minimum critical Rayleigh number (Fig. 11). These objects are larger than the planetesimal radii obtained from astrophysical models (Li et al., 2019; Simon et al., 2016, 2017), thus a non-convecting MG PPB mantle is viable.

The lack of mantle convection also indicates that a mantle structure consisting of a dunitic lower to middle mantle layer overlain by pyroxenitic and/or basaltic upper layers formed by partial differentiation or an inverse depth stratification of primary metal suggested in the previous section would be preserved unless disturbed by impacts. Future space missions to asteroids could potentially investigate such a mantle layering. A warm, but non-convecting, mantle would also be the main reason why the grain size is much larger than accessible mantle samples from Earth (cm versus mm), as Earth has been a dynamic planet throughout its history, thus

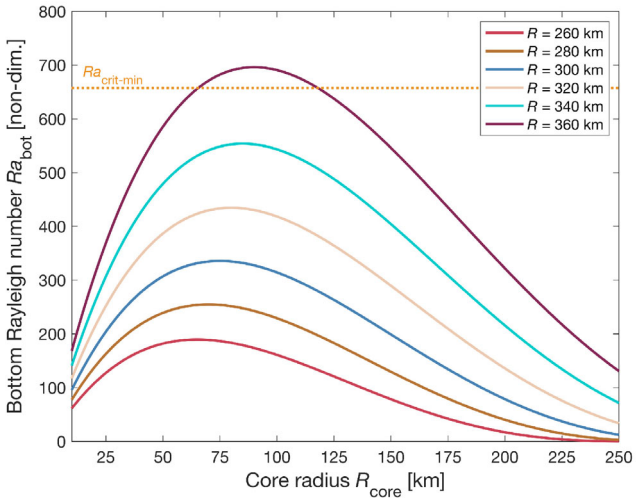

Fig. 11. Bottom Rayleigh number assuming bottom heating of the mantle with core radii ranging from 10 to 250 km. Colored solid lines show calculations for MG PPB radii ranging from 260 to 360 km. The minimum critical Rayleigh number for bottom-heated convection is shown as a dotted orange line. (Color figure can be viewed at wileyonlinelibrary.com.)

Earth's grain size is dictated by the balance between grain growth and dynamic recrystallization (e.g., De Bresser et al., 2001).

Pallasite Formation

Due to their intermediate systematic position between differentiated stone and iron meteorites, pallasites have traditionally been thought to represent the core–mantle boundary region of a planetesimal (e.g., Mittlefehldt et al., 1998), a view still advocated by some authors (e.g., Boesenberg et al., 2012; DellaGiustina et al., 2019). However, the remanent magnetization of inclusions indicates that many pallasites such as Esquel and Imilac were subjected to a magnetic field likely derived from an active core dynamo while cooling below the Curie temperature at approximately 360 °C (Tarduno et al., 2012) that was later confirmed by studies of Fe-Ni metal in the cloudy zones of pallasites using X-ray photoemission electron microscopy (Bryson et al., 2015; Nichols et al., 2021). This is only possible if they were situated in the middle mantle at a sufficient distance from the core and indicated a non-destructive impact for pallasite formation (Solferino & Golabek, 2018; Tarduno et al., 2012). Another recent hypothesis by Johnson et al. (2020) postulates an overpressure buildup in an inwardly crystallizing core causing the formation of dikes that either reach the surface (ferrovolcanism) or form intrusive bodies in the mantle potentially mixing with dunitic material to form pallasites (ferromagmatism). In the present work and our previous publication (Walte et al., 2020), we present new constraints based on textural observations and experimental simulations that confirm the nondestructive two-body impact model and rule out the other models (Table 2). (i) Thin metal-filled secondary veinlets (e.g., Fig. 5) are not texturally equilibrated and indicate a rapid cooling below the Fe-Ni-S solidus of Seymchan and Imilac after the pallasite formation event, as supported by the experimental observation of fast rounding rates of olivine grains while the metal is still molten (Walte et al., 2020). A reasonable fast cooling is also required to prevent longer term gravitational metal-olivine segregation accompanied by olivine–matrix compaction (Walte et al., 2020) and the full re-equilibration of secondary textures in Esquel and Fukang. These conditions are not compatible with a position close to the core–mantle boundary of a liquid core as has been realized for a long time (the "pallasite problem"; e.g., Mittlefehldt et al., 1998; Wahl, 1965). (ii) Small olivine fragments in large primary metal pockets (Fig. 8), the interplay between primary and secondary features in Esquel and Fukang (Fig. 6), and the mechanics of olivine–metal mixing during pallasite formation which is explained best with molten primary metal (Walte et al., 2020) indicate a warm mantle prior to the pallasite formation event. This observation disproves the ferromagmatism hypothesis (Johnson et al., 2020), as the overpressure needed to form dikes from the core into the mantle would require a largely crystallized core (Johnson et al., 2020), related to a colder mantle below the Fe-Ni-S solidus. If core-diking penetrated a warm mantle, for example, facilitated by impacts, no mechanism for the rapid cooling would be available. The textural evidence, namely an initially warm mantle that rapidly cooled after mixing with secondary metal melt followed by slow cooling at lower temperature (700–400 °C) is, however, compatible with a fully destructive impact forming a pallasite planetesimal that was suggested by Yang et al. (2010). The problem of this model is that the lack of a convecting core removes the most likely source of the remanent magnetization. Hence, a non-destructive impact remains the most likely cause for pallasite formation. Fast initial cooling could have been caused by a position close to the surface after the impact, followed by burial with impact regolith (Walte et al., 2020) and/or exogenic material during ongoing accretion. The impactor's core metal would mix into the mantle of the PPB that already contained 2–15 vol% of primary metal, either stranded during partial core–mantle differentiation (Walte et al., 2020) or derived from earlier impacts as discussed above. The core of the pallasite-forming impactor has been suggested to be partially solidified by approximately 80% in order to explain the low Ir concentration of pallasite metal (e.g., Tarduno et al., 2012). Until now, no systematic chemical analyses

Table 2. Compilation of available constraints for the formation of the main group pallasites.

Formation model	Remanent magnetization	**Warm mantle**[a]	**Fast cooling** (≥980 °C range)	Slow cooling (700–400 °C range)	**Varying burial depths**[b]	Low Ir concentration[c]
Core-mantle boundary	No	Yes	No	Yes	No	Yes
Destructive two-body collision	No	Yes	Yes	Yes	Yes	Yes
Ferrovolcanism	No[d]	No	No	Yes	Yes	Yes
Non-destructive two-body collision	Yes	Yes	Yes[e]	Yes[f]	Yes	Yes[g]

Bold text indicates textural constraints from this work and from Walte et al. (2020). The colored boxes indicate whether the constraints are fulfilled (green) or not fulfilled (red) by the different models.

[a]Prior to pallasite formation.

[b]Indicated by this work and by metallographic cooling rates (Yang et al., 2010).

[c]Metal from largely solidified core (~80%) of PPB or of impactor's core (in case of nondestructive collision).

[d]A largely solidified inner core is unlikely to cause long-term dynamo activity.

[e]Rapid cooling after impact by exposure close to surface, for example, after impact rebound (Walte et al., 2020).

[f]Retarded cooling at lower temperatures after formation of an insulating megaregolith layer (Walte et al., 2020) or by ongoing (pebble) accretion.

[g]Secondary metal of impactor; no data available for primary metal.

(Color table can be viewed at wileyonlinelibrary.com.)

for primary metal pockets are available; however, if they remained after partial differentiation, a higher Ir concentration may be expected as more mobile sulfur-rich metal already segregated to form a small core according to this hypothesis. If intruded by earlier impacts, primary metal pockets may show a different but non-predictable trace element composition depending on the impactors. However, in both cases, the trace elements and isotopes of the primary metal pockets should be in chemical equilibrium with the surrounding olivine grains due to the common grain growth history at high temperature, which is not required for the secondary metal that intruded from the pallasite-forming impactor. However, future analysis of primary metal presents a sampling challenge, as contamination through secondary fractures is a possibility (including the missing third dimension of common pallasite sections).

CONCLUSIONS

Our investigation of olivine aggregates found in MG pallasites Seymchan, Imilac, Esquel, and Fukang revealed an inverse relation between grain size and primary metal pockets that is interpreted as a primary feature of PPB mantles. We argue that the primary metal was either heterogeneously distributed throughout the dunitic parts of the mantle or inversely stratified with depth and explain the grain-size variation among the different pallasites by Zener pinning inhibited static grain growth in a warm, but non-convecting mantle. An impactor terminated the olivine grain growth and led to pallasite formation by the influx of the impactor core melt as suggested by previous authors (Bryson et al., 2015; Tarduno et al., 2012; Walte et al., 2020). The mantle was likely still warm before the impact as indicated by largely molten primary metal pockets, which disproves the ferromagmatism hypothesis for pallasite formation (Johnson et al., 2020; note that the general viability of extrusive ferrovolcanism is not affected by our results). After the impact, Seymchan and Imilac cooled rapidly as suggested previously, likely by exposure near the surface (Walte et al., 2020), whereas Fukang and Esquel took more time to cool indicating deeper burial even though the temperature profile, and hence burial depth, cannot be quantified currently. In conclusion, the results of our investigations of olivine aggregates confirm the two-stage model of Walte et al. (2020) for pallasite formation or could indicate an even more complex multi-impact history and provide new constraints for the composition and evolution of planetesimals. Both of these hypotheses described above are principally compatible with a partly differentiated planetesimal with a relatively small core (Walte et al., 2020) and a PPB consisting of a thin mantle overlying a relatively large core (e.g., Nichols et al., 2021). Further experimental work is required to quantify cooling of the different pallasites and to provide input data for both thermal and impact models of planetesimal evolution.

Acknowledgments—We dedicate this paper to Prof. Edward Scott, who pioneered detailed textural investigations of pallasite meteorites. We thank Yves Marrocchi for editorial handling and two anonymous reviewers, whose constructive comments led to improvements of the manuscript. This project would not have been possible without the help of scientists, curators, and photographers of several museums and collections of natural history, who provided detailed photographs of some of the largest and most beautiful pallasite sections known. We thank Dolores Hill and Daniella DellaGiustina, University of Arizona, Lunar &

Planetary Laboratory, Tucson, USA (Fukang main mass); Natasha Almeida, National History Museum, London (Imilac main mass); Denton Ebel, Samuel Alpert, and Denis Finnin, American Museum of Natural History (two Esquel slabs and one Seymchan slab); and Peter Davidson, National Museums of Scotland (Esquel slab). NW acknowledges support from the German Ministry of Education and Research (grant 05K19WCA). Open Access funding enabled and organized by Projekt DEAL.

Data Availability Statement—The data that support the findings of this study are available from the corresponding author upon reasonable request.

Editorial Handling—Dr. Yves Marrocchi

REFERENCES

Bagdassarov, N., Golabek, G. J., Solferino, G., and Schmidt, M. W. 2009. Constraints on the Fe-S Melt Connectivity in Mantle Silicates from Electrical Impedance Measurements. *Physics of the Earth and Planetary Interiors* 177: 139–46.

Barrat, J.-A., and Ferrière, L. 2021. Olivines in Main-Group Pallasites: Magma-Ocean Cumulates or Partial Melting Residues? *Geochemical Perspectives Letters* 16: 47–52.

Boesenberg, J. S., Delaney, J. S., and Hewins, R. H. 2012. A Petrological and Chemical Reexamination of Main Group Pallasite Formation. *Geochimica et Cosmochimica Acta* 89: 134–58.

Bryson, J. F. J., Nichols, C. I. O., Herrero-Albillos, J., Kronast, F., Kasama, T., Alimadadi, H., van der Laan, G., Nimmo, F., and Harrison, R. J. 2015. Long-Lived Magnetism from Solidification-Driven Convection on the Pallasite Parent Body. *Nature* 517: 472–5.

Buseck, P. R. 1977. Pallasite Meteorites—Mineralogy, Petrology and Geochemistry. *Geochimica et Cosmochimica Acta* 41: 711–40.

De Bresser, J. H. P., Ter Heege, J. H., and Spiers, C. J. 2001. Grain Size Reduction by Dynamic Recrystallization: Can it Result in Major Rheological Weakening? *International Journal of Earth Sciences* 90: 28–45.

DellaGiustina, D. N., Habib, N., Domanik, K. J., Hill, D. H., Lauretta, D. S., Goreva, Y. S., Killgore, M., Hexiong, Y., and Downs, R. T. 2019. The Fukang Pallasite: Characterization and Implications for the History of the Main-Group Parent Body. *Meteoritics & Planetary Science* 54: 1781–807.

Faul, U. H., and Scott, D. 2006. Grain Growth in Partially Molten Olivine Aggregates. *Contributions to Mineralogy and Petrology* 151: 101–11.

German, R. M. 2010. Coarsening in Sintering: Grain Shape Distribution, Grain Size Distribution, and Grain Growth Kinetics in Solid-Pore Systems. *Critical Reviews in Solid State and Materials Sciences* 35: 263–305.

Greenwood, R. C., Barrat, J.-A., Scott, E. R. D., Haack, H., Buchanan, P. C., Franchi, I. A., Yamaguchi, A., Johnson, D., Bevan, A. W. R., and Burbine, T. H. 2015. Geochemistry and Oxygen Isotope Composition of Main-Group Pallasites and Olivine-Rich Clasts in Mesosiderites: Implications for the "Great Dunite Shortage" and HED-Mesosiderite Connection. *Geochimica et Cosmochimica Acta* 169: 115–36.

Hiraga, T., Tachibana, C., Ohashi, N., and Sano, S. 2010. Grain Growth Systematics for Forsterite ± Enstatite Aggregates: Effect of Lithology on Grain Size in the Upper Mantle. *Earth and Planetary Sciences Letters* 291: 10–20.

Hustoft, J., Scott, T., and Kohlstedt, D. L. 2007. Effect of Metallic Melt on the Viscosity of Peridotite. *Earth and Planetary Sciences Letters* 260: 355–60.

Johnson, B. C., Sori, M. M., and Evans, A. J. 2020. Ferrovolcanism on Metal Worlds and the Origin of Pallasites. *Nature Astronomy* 4: 41–4.

Karato, S.-I., and Wu, P. 1993. Rheology of the Upper Mantle: A Synthesis. *Science* 260: 771–8.

Kohlstedt, D. L., and Holtzman, B. K. 2009. Shearing Melt Out of the Earth: An Experimentalist's Perspective on the Influence of Deformation on Melt Extraction. *Annual Review of Earth and Planetary Sciences* 37: 561–93.

Kong, M., Bhattacharya, R. N., James, C., and Basu, A. 2005. A Statistical Approach to Estimate the 3D Size Distribution of Spheres from 2D Size Distributions. *Geological Society of America Bulletin* 117: 244–9.

Li, R., Youdin, A. N., and Simon, J. B. 2019. Demographics of Planetesimals Formed by the Streaming Instability. *The Astrophysical Journal* 885: 69.

Lichtenberg, T., Keller, T., Katz, R. E., Golabek, G. J., and Gerya, T. V. 2019. Magma Ascent in Planetesimals: Control by Grain Size. *Earth and Planetary Sciences Letters* 507: 154–65.

Llorens, M.-G., Gomez-Rivas, E., Ganzhorn, A.-C., Griera, A., Steinbach, F., Roessiger, J., Labrousse, L., Walte, N. P., Weikusat, I., and Bons, P. D. 2019. The Effect of Dynamic Recrystallisation on the Rheology and Microstructures of Partially Molten Rocks. *Journal of Structural Geology* 118: 224–35.

Manthilake, M. A. G. M., Walte, N., and Frost, D. J. 2012. A New Multi-Anvil Press Employing Six Independently Acting 8 MN Hydraulic Rams. *High Pressure Research* 32: 195–207.

McKibbin, S. J., Pittarello, L., Makarona, C., Hamann, C., Hecht, L., Chernonozhkin, S. M., Goderis, S., and Clayes, P. 2019. Petrogenesis of Main Group Pallasite Meteorites Based on Relationships Among Texture, Mineralogy, and Geochemistry. *Meteoritics & Planetary Science* 54: 2814–44.

Minarik, W. G., Ryerson, F. J., and Watson, E. B. 1996. Textural Entrapment of Core-Forming Melts. *Science* 272: 530–3.

Mittlefehldt, D. W., McCoy, T. J., Goodrich, C. A., and Kracher, A. 1998. Non-Chondritic Meteorites from Asteroidal Bodies. In *Planetary Materials*, vol. 36, edited by J. J. Papike, 4-1–195. Chantilly, Virginia: Mineralogical Society of America.

Néri, A., Guignard, J., Monnereau, M., Bystricky, M., Perrillat, J.-P., Andrault, D., King, A., Guignot, N., Tenailleau, C., Duployer, B., Toplis, M. J., and Quitté, G. 2020. Reevaluation of Metal Interconnectivity in a Partially Molten Silicate Matrix Using 3D Micro-tomography. *Physics of the Earth and Planetary Interiors* 308: 106571.

Nichols, C. I. O., Bryson, J. F. J., Cottrell, R. D., Fu, R. R., Harrison, R. J., Herrero-Albillos, J., Kronast, F., Tarduno, J. A., and Weiss, B. P. 2021. A Time-Resolved Paleomagnetic Record of Main Group Pallasites: Evidence

for a Large-Cored, Thin-Mantled Parent Body. *Journal of Geophysical Research: Planets* 126: e2021JE006900.
Scott, E. R. D. 1977. Formation of Olivine-Metal Textures in Pallasite Meteorites. *Geochimica et Cosmochimica Acta* 41: 693–710.
Scott, E. R. D. 2017. Pallasites: Olivine-Metal Textures, Metal Compositions, Minor Phases, Origins, and Insights into Processes at Core-Mantle Boundaries of Asteroids (Abstract #1037). 47th Lunar and Planetary Science Conference. CD-ROM.
Simon, J. B., Armitage, P. J., Li, R., and Youdin, A. N. 2016. The Mass and Size Distribution of Planetesimals Formed by the Streaming Instability. I. The Role of Self-Gravity. *The Astrophysical Journal* 822: 55.
Simon, J. B., Armitage, P. J., Youdin, A. N., and Li, R. 2017. Evidence for Universality in the Initial Planetesimal Mass Function. *The Astrophysical Journal Letters* 847: l12.
Smith, C. S. 1948. Grains, Phases and Interfaces: An Interpretation of Microstructure. *Transactions of the Metallurgical Society of AIME* 175: 15–51.
Solferino, G. F. D., and Golabek, G. J. 2018. Olivine Grain Growth in Partially Molten Fe-Ni-S: A Proxy for the Genesis of Pallasite Meteorites. *Earth and Planetary Sciences Letters* 504: 38–52.
Solferino, G. F. D., Golabek, G. J., Nimmo, F., and Schmidt, M. W. 2015. Fast Grain Growth of Olivine in Liquid Fe-S and the Formation of Pallasites with Rounded Olivine Grains. *Geochimica et Cosmochimica Acta* 162: 259–75.
Solferino, G. F. D., Thomson, P.-R., and Hier-Majumder, S. 2020. Pore Network Modeling of Core Forming Melts in Planetesimals. *Frontiers in Earth Science* 8: 339.
Tarduno, J. A., Cottrell, R. D., Nimmo, F., Hopkins, J., Voronov, J., Erickson, A., Blackman, E., Scott, E. R. D., and McKinley, R. 2012. Evidence for a Dynamo in the Main Group Pallasite Parent Body. *Science* 338: 939–42.
Turcotte, D. L., and Schubert, G. 2014. *Geodynamics*, 3rd ed., New York: Cambridge University Press.
Ulff-Møller, F., Choi, B. G., Rubin, A. E., Tran, J., and Wasson, J. T. 1998. Paucity of Sulfide in a Large Slab of Esquel: New Perspectives on Pallasite Formation. *Meteoritics & Planetary Science* 33: 221–7.
Wahl, W. 1965. The Pallasite Problem. *Geochimica et Cosmochimica Acta* 29: 177–81.
Walte, N. P., Becker, J. K., Bons, P. D., Rubie, D. C., and Frost, D. J. 2007. Liquid-Distribution and Attainment of Textural Equilibrium in a Partially-Molten Crystalline System with a High-Dihedral-Angle Liquid Phase. *Earth and Planetary Sciences Letters* 262: 517–32.
Walte, N. P., Bons, P. D., Passchier, C. W., and Koehn, D. 2003. Disequilibrium Melt Distribution During Static Recrystallization. *Geology* 31: 1009–12.
Walte, N. P., Rubie, D. C., Bons, P. D., and Frost, D. J. 2011. Deformation of a Crystalline Aggregate with a Small Percentage of High-Dihedral-Angle Liquid: Implications for Core-Mantle Differentiation During Planetary Formation. *Earth and Planetary Sciences Letters* 305: 124–34.
Walte, N. P., Solferino, G. F. D., Golabek, G. J., Silva Souza, D., and Bouvier, A. 2020. Two-Stage Formation of Pallasites and the Evolution of Their Parent Bodies Revealed by Deformation Experiments. *Earth and Planetary Sciences Letters* 546: 116419.
Wasson, J. T., and Choi, B. G. 2003. Main-Group Pallasites: Chemical Composition, Relationship to IIIAB Irons, and Origin. *Geochimica et Cosmochimica Acta* 67: 3079–96.
Yang, J. J., Goldstein, J. I., and Scott, E. R. D. 2010. Main-Group Pallasites: Thermal History, Relationship to IIIAB Irons, and Origin. *Geochimica et Cosmochimica Acta* 74: 4471–92.

SUPPORTING INFORMATION

Additional supporting information may be found in the online version of this article.

Fig. S1. Photographic images of the olivine aggregates that form the basis for the textural drawings in Fig. 2. (a) Seymchan pallasite SEY-18-01. (b) Imilac BM.53322 (© The Trustees of the National History Museum, London). (c) Esquel G.2010.9.1 (© National Museums Scotland, Edinburgh). (d) Esquel #4958 (Credit: Denis Finnin, AMNH). (e) Fukang pallasite (Credit: Dolores Hill, Univ. Arizona, Lunar & Planetary Laboratory).

Fig. S2. Imilac slab BM.53322 of the Natural History Museum, London (© The Trustees of the National History Museum, London). Red ellipses denote olivine aggregates that were analyzed (see Table 1).

Fig. S3. Esquel slab #4972 of the American Museum of Natural History (Credit: Denis Finnin, AMNH). Red ellipses denote olivine aggregates that were analyzed (see Table 1).

Fig. S4. Esquel slab #4958 of the American Museum of Natural History (Credit: Denis Finnin, AMNH). Red ellipses denote olivine aggregates that were analyzed (see Table 1).

Fig. S5. Section of the main mass of Fukang pallasite, property of Marvin and Kitty Killgore of Southwest Meteorite Lab (Credit: Dolores Hill, Univ. Arizona, Lunar & Planetary Laboratory). Red ellipses denote olivine aggregates that were analyzed (see Table 1).